Nonideal Fields Solve the Injection Problem in Relativistic Reconnection

Lorenzo Sironi

Phys. Rev. Lett. **128**, 145102 — Published 8 April 2022

DOI: 10.1103/PhysRevLett.128.145102

Non-ideal fields solve the injection problem in relativistic reconnection

Lorenzo Sironi*
Department of Astronomy and Columbia Astrophysics Laboratory, Columbia University, New York, NY 10027, USA
(Dated: March 23, 2022)

Magnetic reconnection in relativistic plasmas is well established as a fast and efficient particle accelerator, capable of explaining the most dramatic astrophysical flares. With particle-in-cell simulations, we demonstrate the importance of non-ideal fields for the early stages ("injection") of particle acceleration. Most of the particles ending up with high energies (near or above the mean magnetic energy per particle) must have passed through non-ideal regions where the assumptions of ideal magnetohydrodynamics are broken (i.e., regions with $E > B$ or nonzero $E_\parallel = \mathbf{E}\cdot\mathbf{B}/B$), whereas most of the particles that do not experience non-ideal fields end up with Lorentz factors of order unity. Thus, injection by non-ideal fields is a necessary prerequisite for further acceleration. Our results have important implications for the origin of nonthermal particles in high-energy astrophysical sources.

Magnetic reconnection in the relativistic regime [1–3], where the magnetic energy is larger than the particle rest-mass energy (equivalently, the mean magnetic energy per particle is $\sim \sigma mc^2 \gg mc^2$, with σ the magnetization), has been invoked to explain the most dramatic flaring events in astrophysical high-energy sources [e.g. 4–11]. Our understanding of the physics of relativistic reconnection has greatly advanced thanks to fully-kinetic particle-in-cell (PIC) simulations, which have established reconnection as an efficient particle accelerator [e.g. 12–16]. It is widely accepted that most of the energy gain of ultra-relativistic particles comes from ideal fields [e.g. 13, 17]. It was then argued that the spectrum of high-energy particles would remain unchanged, if non-ideal fields were to be ignored [17].

In this *Letter*, we demonstrate that, instead, non-ideal fields have a key role in the acceleration process. They are essential for solving the "injection problem," so that non-relativistic particles can be promoted to relativistic ($\sim \sigma mc^2 \gg mc^2$) energies. Injection by non-ideal fields is a necessary prerequisite to access further acceleration channels, primarily governed by ideal fields [13, 16–20]. High-energy particles receive most of their energy by ideal fields (in 2D, via Fermi-like acceleration with the "slingshot" mechanism [17] or via magnetic moment conservation in the increasing field of compressing plasmoids [19, 20]; in 3D, via grad-B-drift acceleration while their orbits sample both sides of the layer [16]). However, we find that most of the particles ending up with high energies (near or above the mean magnetic energy per particle) must have been pre-energized in non-ideal regions, before being further accelerated by ideal fields. We find that if non-ideal fields were artificially excluded, most of the particles would end up with low energies.

Setup—We perform 2D and 3D PIC simulations with TRISTAN-MP [21, 22]. We initialize a force-free field of strength B_0, whose direction rotates from $+\hat{x}$ to $-\hat{x}$ across a current sheet at $y = 0$. We consider a cold electron-positron plasma with rest-frame density n_0 of 16 particles per cell in 2D and 4 in 3D (Suppl. Mat. for convergence studies). Particles initially in the current sheet are excluded from our analysis, so to obtain results independent from specific choices at initialization. The field strength B_0 is parameterized by the magnetization $\sigma = B_0^2/4\pi n_0 mc^2 = (\omega_c/\omega_p)^2$, where $\omega_c = eB_0/mc$ is the Larmor frequency and $\omega_p = \sqrt{4\pi n_0 e^2/m}$ the plasma frequency. We vary σ in the range $3 \lesssim \sigma \lesssim 200$, with $\sigma = 50$ as our reference case. Most of our runs assume a vanishing guide field, but we also present results with guide field $B_g = B_0$ initialized along z as in [23].

Along the y-direction of inflows, two injectors continuously introduce fresh plasma and magnetic flux into the domain, see [24]. We employ periodic boundary conditions in z. Most of our runs have periodic boundaries also in x (but our conclusions also hold for outflow x-boundaries, Suppl. Mat.). Each simulation is evolved for $\sim 2.5\, L_x/c$ (the periodic x-boundaries would artificially choke reconnection at longer times). We usually let reconnection start spontaneously from numerical noise, but we also show similar results when reconnection is "triggered" by hand at the initial time. We resolve the plasma skin depth with $c/\omega_p = 5$ cells, and employ large domains up to $L_x \simeq 6400\, c/\omega_p$ in 2D (our reference is $L_x \simeq 1600\, c/\omega_p$), and $L_x = 2L_z \simeq 800\, c/\omega_p$ in 3D.

Results—Near X-points the reconnected field scales as $B_y \sim B_0\, x/\Delta$ over some length Δ, whereas the electric field is $E_z \sim \eta_{\rm rec} B_0$, with $\eta_{\rm rec} \sim 0.1$ the reconnection rate [e.g., 24]. For $B_g = 0$, magnetic dominance is broken (i.e., $E > B$) at $|x| \lesssim \eta_{\rm rec}\Delta$. For $B_g = 0$ the parallel electric field $E_\parallel = \boldsymbol{E}\cdot\boldsymbol{B}/B$ necessarily vanishes, so non-ideal effects are captured by $E > B$, rather than by $E_\parallel$. In contrast, in the presence of a nonzero B_g, the region of electric dominance disappears if $B_g/B_0 \gtrsim \eta_{\rm rec}$. Here, $E_\parallel \sim \eta_{\rm rec} B_0$ near the X-point, i.e., the electric field is entirely accounted for by $E_\parallel$. Thus, non-ideal effects are captured by $E > B$ for $B_g/B_0 \lesssim \eta_{\rm rec}$, and by $E_\parallel$ for stronger guide fields. We verified this argument with a sweep of B_g/B_0 values, but here we focus only on $B_g = 0$

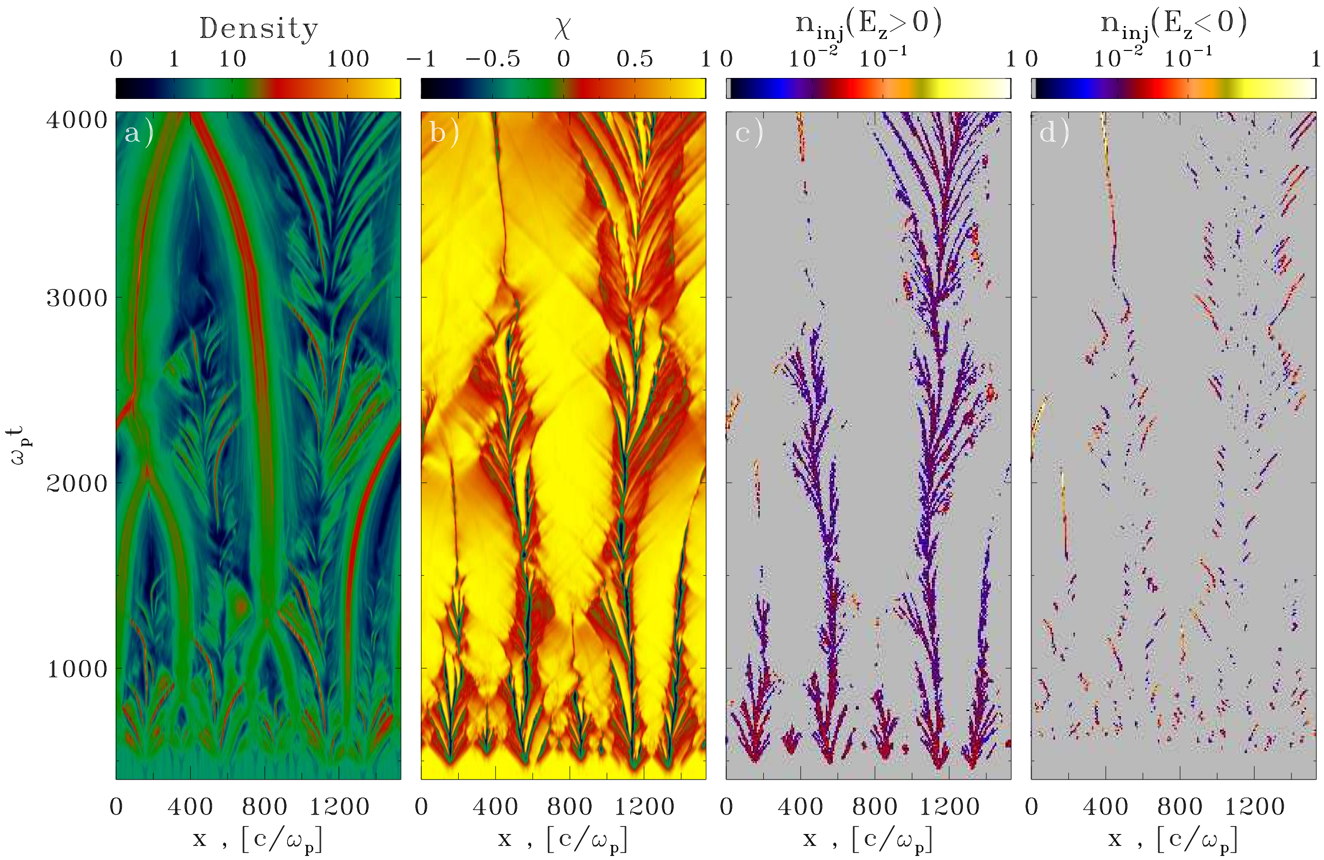

FIG. 1. Evolution of the layer for our reference simulation ($\sigma = 50,\ B_g = 0,\ L_x = 1600\,c/\omega_{\rm p}$). (a) Density in the midplane $y = 0$, normalized to n_0; (b) $\chi = (B^2 - E^2)/(B^2 + E^2)$ at $y = 0$, to identify regions of magnetic ($\chi > 0$) or electric ($\chi < 0$) dominance; the particle x-locations at their first $E > B$ encounter are shown in (c) and (d), where we distinguish between particles that experience $E > B$ with $E_z > 0$ (c) vs $E_z < 0$ (d) (see text).

(our main case) and $B_g/B_0 = 1$.

The layer evolution for our reference simulation ($\sigma = 50,\ B_g = 0,\ L_x = 1600\,c/\omega_{\rm p}$) is shown in Fig. 1(a), where we present the spatio-temporal structure of density in the midplane ($y = 0$). At early times, the layer breaks into a series of primary plasmoids. Over time, they grow and coalesce, and new secondary plasmoids appear in the under-dense regions in-between primary plasmoids (e.g., top right in Fig. 1(a)). Regions with $E > B$ are rather ubiquitous in between plasmoids (see the green and blue areas in Fig. 1(b), where we plot $\chi = (B^2-E^2)/(B^2+E^2)$ at $y = 0$). For each simulation particle, we detect the first time (if any) it experiences $E > B$, and record its position at this time. The particle x-locations at their first $E > B$ encounter are shown in panels (c) and (d), where we distinguish between particles that experience $E > B$ with $E_z > 0$ (c) vs $E_z < 0$ (d). The former ($E_z > 0$) is expected for X-points of the main layer, whereas $E_z < 0$ in between merging plasmoids, as demonstrated by comparing (c) and (d) with (a).

The high-energy part of the spectrum extracted from the reconnection region [25] is dominated by particles that experienced $E > B$ at some point in their history. In Fig. 2, we plot the overall spectrum with solid lines, the spectrum of particles that experienced $E > B$ (hereafter, "$E > B$ particles") with dashed lines, and the spectrum of particles that never experienced $E > B$ (hereafter, "$E < B$ particles") with dotted lines. "$E > B$ particles" are particles that at some point experienced $E > B$, so they are not only those currently in $E > B$ regions.

For high magnetizations, the high-energy tail of the spectrum is mostly populated by $E > B$ particles, regardless of system size (Fig. 2(a) [26]) and dimensionality (inset in Fig. 2(a), showing a comparison between 2D and 3D). With increasing σ (Fig. 2(b)), the spectrum of $E > B$ particles shifts to higher energies as $\propto \sigma$ (see inset in Fig. 2(b), where $\gamma - 1$ on the horizontal axis is rescaled by $(50/\sigma)$), and it increases in normalization. In contrast, the spectrum of $E < B$ particles peaks at $\gamma - 1 \sim$ few for all magnetizations, and at high energies it drops much steeper than the $E > B$ spectrum. Thus, the overall spectrum can be described as a combination of two populations: a low-energy peak at trans-relativistic energies contributed by $E < B$ particles, and a high-

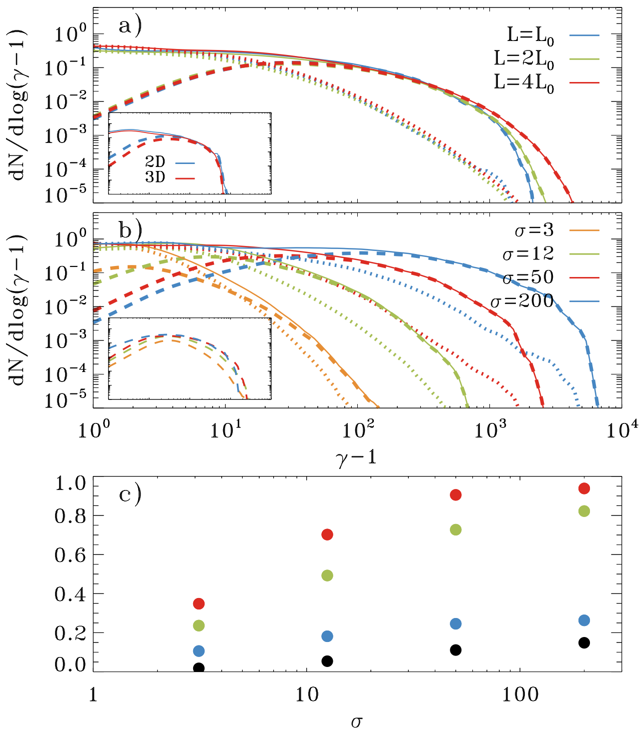

FIG. 2. (a) Particle spectra at $t \simeq 1.8\, L_x/c$ (solid lines), for simulations with $\sigma = 50$, $B_g = 0$ and different box sizes: $L_x = L_0 = 1600\, c/\omega_{\rm p}$ (blue), $L_x = 2L_0 = 3200\, c/\omega_{\rm p}$ (green), and $L_x = 4L_0 = 6400\, c/\omega_{\rm p}$ (red). Dashed lines show the spectrum $E > B$ particles (see text), dotted lines of $E < B$ particles. Inset: comparison of 2D and 3D triggered simulations with $\sigma = 50$, $B_g = 0$, $L_x = 400\, c/\omega_{\rm p}$ at $t \simeq 1{,}000\, \omega_{\rm p}^{-1} \simeq 2.5 L_x/c$. Dashed and solid lines as in the main panel. (b) Spectra at $t \simeq 4000\, \omega_{\rm p}^{-1} \simeq 2.5 L_x/c$ for simulations with $L_x = 1600\, c/\omega_{\rm p}$, $B_g = 0$ and varying σ, see the legend; line style as in (a). The inset presents the spectra of $E > B$ particles, but $\gamma - 1$ on the horizontal axis is rescaled by $(50/\sigma)$. (c) Contribution of $E > B$ particles to the total census in the reconnection region (blue), and to the number of particles with $\gamma > \sigma/4$ (green) and $\gamma > \sigma$ (red), as a function of σ. The black points show the fraction of length along $y = 0$ occupied by $E > B$ regions.

energy bump with mean Lorentz factor $\propto \sigma$ populated by $E > B$ particles.

A robust result of PIC simulations is that higher magnetizations display harder spectra, with $p = -d\log N/d\log\gamma \to 1$ for $\sigma \gg 1$ [e.g. 12–15]. For domain sizes within the reach of current PIC simulations, the spectrum does not extend much beyond the post-injection spectrum (the cutoff is at $\lesssim 10\,\sigma mc^2$ [16, 19, 20]; indeed, hard power-laws with $p < 2$ could not extend to much higher energies without running into an energy crisis [19]). The fact that higher magnetizations display harder spectra has a simple explanation. While the peak of the $E < B$ population is nearly σ-independent, the $E > B$ component shifts to higher energies ($\sim \sigma mc^2$) and higher normalizations with increasing σ, thus hardening the overall spectrum (Fig. 2(b)).

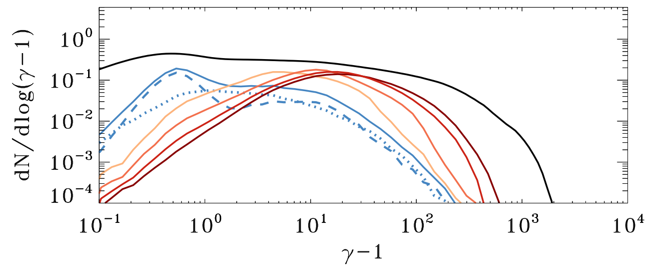

FIG. 3. Evidence of fast energization near non-ideal regions, for $\sigma = 50$, $B_g = 0$ and $L_x = 1600\, c/\omega_{\rm p}$. The spectrum of particles at their first $E > B$ encounter is shown by the dashed blue line if $E_z > 0$, and dotted blue if $E_z < 0$. Their sum is the solid blue. The series of spectra from light to dark red are measured, for those same particles, respectively $\sim 9, 27, 90, 270\ \omega_{\rm p}^{-1}$ after their first $E > B$ encounter. For comparison, the black line shows the overall spectrum at the final time $\omega_{\rm p} t \simeq 4000$.

In the asymptotic limit $\sigma \gg 1$, $E > B$ particles contribute a fraction $\gtrsim 90\%$ at $\gamma > \sigma$ (red points in Fig. 2(c)) and $\gtrsim 70\%$ at $\gamma > \sigma/4$ (green). These fractions are nearly constant in time for $t \gtrsim L_x/c$ (Suppl. Mat.), and independent of the domain size (Fig. 2(a)). For $\sigma \gtrsim 50$, $E > B$ particles account for $\sim 20\%$ of the overall census in the reconnection region (Fig. 2(c), blue). This can be related to the fraction of length along the $y = 0$ line (of area in the $y = 0$ plane, for 3D) occupied by non-ideal regions, as we now explain.

The black points in Fig. 2(c) denote the "occupation fraction" of $E > B$ regions along $y = 0$, averaged over $1 \lesssim ct/L_x \lesssim 2$. This fraction increases with σ [27], and in the limit $\sigma \gg 1$ approaches $\sim 10\%$ (black points in Fig. 2(c)), which is about half of the fraction of $E > B$ particles (blue).

This factor of two has a simple explanation. The dashed blue line in Fig. 3 shows the spectrum measured, for each particle, at its first $E > B$ encounter with $E_z > 0$, as appropriate for X-points in the main layer. It contains $\sim 10\%$ of post-reconnection particles, i.e., exactly equal to the $E > B$ occupation fraction. The dotted blue line in Fig. 3, instead, shows the spectrum of particles experiencing $E > B$ with $E_z < 0$, i.e., in between merging plasmoids. It also contains $\sim 10\%$ of particles. Thus, for $\sigma \gtrsim 50$, $\sim 10\%$ of particles encounter $E > B$ fields when entering the reconnection region, and an additional $\sim 10\%$ in secondary layers between merging plasmoids. The latter extend along y, so their X-points are not accounted for by the black markers in Fig. 2(c). This justifies why for $\sigma \gtrsim 50$ the fraction of $E > B$ particles (blue in Fig. 2(c)) is twice larger than the $E > B$ occupation fraction (black).

In Fig. 3, we provide evidence of fast particle acceleration near non-ideal regions. The spectrum of particles

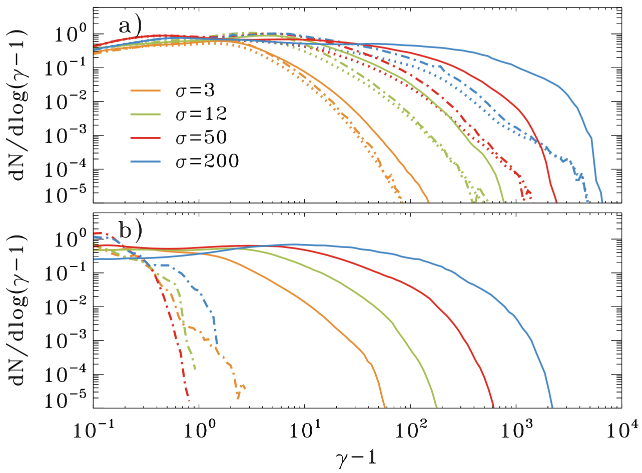

FIG. 4. Experiments with test-particles that do not experience non-ideal fields, for $B_g = 0$ (top) and $B_g = B_0$ (bottom). Spectra are computed at $\omega_{\rm p} t = 4000$ for simulations with $L_x = 1600\, c/\omega_{\rm p}$ and varying σ (see legend). Top: solid and dotted lines as in Fig. 2(b), whereas dash-dotted lines present the final spectrum of test-particles. They are initialized as regular particles, but when they pass through $E > B$ regions, we artificially fix their Lorentz factor at $\gamma - 1 \sim$ few (more specifically, to the same peak as the dotted lines). Bottom: solid lines for regular particles, while dash-dotted lines for test-particles evolved without the contribution by $E_\parallel$.

at their first $E > B$ encounter is shown by the solid blue line, demonstrating that at this point the particles still have low energies. The series of spectra from light to dark red are measured, for those same particles, respectively $\sim$ 9, 27, 90, 270 $\omega_{\rm p}^{-1}$ after their first $E > B$ encounter. The spectral peak quickly shifts up to $\gamma - 1 \sim 5$ (first red line; at this time, most of the particles are still in $E > B$ regions), yielding a mean acceleration rate $d\gamma/dt \sim 0.5\, \omega_{\rm p}^{-1}$, comparable to the maximal rate $\sim \eta_{\rm rec} |\beta_z| \sqrt{\sigma} \omega_{\rm p}^{-1}$ [16] assuming a z-velocity $|\beta_z| \simeq 0.7$ (particles accelerated at X-points also have some β_x along the outflow). Rapid acceleration continues up to $\gamma - 1 \simeq 20 \sim \sigma/2$ (third red line) [28]. Beyond this stage, the spectrum still shifts up in energy [19, 20], but at a slower rate (compare the two darkest red lines). The later stages are governed by ideal fields [17].

To corroborate our conclusions on the importance of non-ideal fields for particle injection, we present in Fig. 4 two additional experiments. For $3 \lesssim \sigma \lesssim 200$, we analyze the cases of vanishing ($B_g = 0$, top) and strong ($B_g = B_0$, bottom) guide fields. The final spectra are indicated by solid lines. In the top panel, dotted lines show the spectra of $E < B$ particles, whereas dash-dotted lines the spectra of "test-particles" — not contributing to the electric currents in the simulation, but otherwise initialized and evolved as regular particles. When test-particles pass through $E > B$ regions, we artificially fix their Lorentz factor at $\gamma - 1 \sim$ few. The remarkable agreement between dash-dotted and dotted lines demonstrates that if we do not allow test-particles to gain energy while in $E > B$ regions, they display similar spectra as particles that never had $E > B$ encounters (we have confirmed this also for the 3D simulation of Fig. 2(a), inset). The high-energy spectra of test-particles (dash-dotted lines) are much steeper than the ones of regular particles (solid lines). Equivalently, energization in non-ideal regions plays a key role in shaping the high-energy end of the particle spectrum.

Fig. 4(b) refers instead to $B_g = B_0$. As we discussed, here non-ideal effects are well captured by $E_\parallel$. Comparison with Fig. 4(a) shows that spectra are softer for larger B_g. The fraction of injected particles decreases with increasing B_g/B_0 because the layer is less prone to fragmentation into plasmoids [29, 30], and so to formation of non-ideal regions. In Fig. 4(b), dash-dotted lines present the spectrum of test-particles evolved without $E_\parallel$, so in response to $\boldsymbol{E} - E_\parallel (\boldsymbol{B}/B)$. When inhibiting energization by $E_\parallel$, the test-particles stay at non-relativistic energies.

Conclusions—We investigate the injection physics of particle acceleration in relativistic reconnection. In contrast to earlier claims [17], we find that energization by non-ideal fields is a necessary prerequisite for further acceleration (in Suppl. Mat. we compare to [17], showing that their conclusions were misled by an initial transient phase where $E < B$ particles may dominate). Most of the particles that are artificially evolved without non-ideal fields do not even reach relativistic energies. We then argue that studies of reconnection-powered acceleration that employ test-particles in magnetohydrodynamics simulations need to properly include non-ideal fields. Such studies may prove useful to validate our conclusions in larger domains, beyond the reach of PIC simulations.

The spectral component of particles that encountered non-ideal regions shifts to greater energies ($\sim \sigma m c^2$) and higher normalizations with increasing magnetization, whereas particles that do not experience non-ideal fields always end up with Lorentz factors near unity. The overall spectrum then gets harder for higher σ, which explains the σ-dependent spectral hardness reported in PIC simulations [e.g., 13–15]. This statement applies to the range $1 \lesssim \gamma \lesssim 10\,\sigma$ of the post-injection spectrum. At higher energies, an additional power-law tail will emerge, whose slope is set by the dominant acceleration mechanism, which is different between 2D [20, 31] and 3D [16].

Finally, we remark that, even though we have assumed an electron-positron plasma, it is well known that $\sigma \gg 1$ reconnection behaves similarly in electron-positron, electron-proton [32–34] and electron-positron-proton [35] plasmas, so our results should apply regardless of the plasma composition. The importance of non-ideal fields for particle injection has also been emphasized in studies of non-relativistic low-beta turbulence and reconnection [36–39] and magnetically-dominated turbulence [40].

We thank L. Comisso, D. Groselj, A. Spitkovsky and N. Sridhar for comments that greatly improved the clarity of the paper. We thank F. Guo for discussions on this topic. L.S. acknowledges support from the Cottrell Scholars Award, NASA 80NSSC20K1556, NSF PHY-1903412, DoE DE-SC0021254 and NSF AST-2108201. This project made use of the following computational resources: NASA Pleiades supercomputer, Habanero and Terremoto HPC clusters at Columbia University. This work is dedicated to the memory of my father.

* lsironi@astro.columbia.edu

[1] M. Lyutikov and D. Uzdensky, ApJ **589**, 893 (2003).
[2] Y. E. Lyubarsky, MNRAS **358**, 113 (2005).
[3] L. Comisso and F. A. Asenjo, Phys. Rev. Lett. **113**, 045001 (2014), 1402.1115.
[4] B. Cerutti, G. R. Werner, D. A. Uzdensky, and M. C. Begelman, ApJ **770**, 147 (2013).
[5] Y. Yuan, K. Nalewajko, J. Zrake, W. E. East, and R. D. Blandford, ApJ **828**, 92 (2016).
[6] M. Lyutikov, S. Komissarov, L. Sironi, and O. Porth, JPlPh **84**, 635840201 (2018).
[7] M. Petropoulou, D. Giannios, and L. Sironi, MNRAS **462**, 3325 (2016).
[8] J. Ortuño-Macías and K. Nalewajko, MNRAS **497**, 1365 (2020).
[9] I. M. Christie, M. Petropoulou, L. Sironi, and D. Giannios, MNRAS **482**, 65 (2019).
[10] J. M. Mehlhaff, G. R. Werner, D. A. Uzdensky, and M. C. Begelman, MNRAS (2020).
[11] D. N. Hosking and L. Sironi, ApJ **900**, L23 (2020), 2007.14992.
[12] S. Zenitani and M. Hoshino, ApJL **562**, L63 (2001).
[13] L. Sironi and A. Spitkovsky, ApJL **783**, L21 (2014).
[14] F. Guo, H. Li, W. Daughton, and Y.-H. Liu, PhRvL **113**, 155005 (2014).
[15] G. R. Werner, D. A. Uzdensky, B. Cerutti, K. Nalewajko, and M. C. Begelman, ApJL **816**, L8 (2016).
[16] H. Zhang, L. Sironi, and D. Giannios, arXiv e-prints arXiv:2105.00009 (2021), 2105.00009.
[17] F. Guo, X. Li, W. Daughton, P. Kilian, H. Li, Y.-H. Liu, W. Yan, and D. Ma, The Astrophysical Journal **879**, L23 (2019), 1901.08308.
[18] K. Nalewajko, D. A. Uzdensky, B. Cerutti, G. R. Werner, and M. C. Begelman, ApJ **815**, 101 (2015).
[19] M. Petropoulou and L. Sironi, MNRAS **481**, 5687 (2018).
[20] H. Hakobyan, M. Petropoulou, A. Spitkovsky, and L. Sironi, Astrophys. J. **912**, 48 (2021), 2006.12530.
[21] O. Buneman, Computer Space Plasma Physics: Simulation Techniques and Softwares (1993).
[22] A. Spitkovsky, in *Simulations of relativistic collisionless shocks: shock structure and particle acceleration*, edited by T. Bulik, B. Rudak, & G. Madejski (2005), vol. 801 of *AIP Conf. Ser.*, p. 345.
[23] P. Kilian, X. Li, F. Guo, and H. Li, Astrophys. J. **899**, 151 (2020), 2001.02732.
[24] L. Sironi, D. Giannios, and M. Petropoulou, MNRAS **462**, 48 (2016).
[25] Note1, we define the reconnection region such that it contains a mixture of particles starting from $y > 0$ and $y < 0$ [41], with both populations contributing at least 10% (our results do not significantly depend on this fraction). Unless otherwise noted, we only show the spectrum of particles belonging to the reconnection region.
[26] Note2, the shift of the spectral cutoff to higher energies with increasing system size has been extensively characterized, in both 2D [15, 19, 20] and 3D [16].
[27] Note3, the increase with σ has two reasons: first, fragmentation of the layer by the secondary plasmoid instability [42] is more pronounced for higher σ, increasing the number of non-ideal regions [24]; second, a given $E > B$ region is more extended at higher σ, since $\eta_{\rm rec}$ increases with magnetization [43]. Both effects reach an asymptotic limit at $\sigma \gtrsim 50$.
[28] Note4, as we show in Suppl. Mat., this is also the peak of the spectrum of particles currently residing in $E > B$ regions.
[29] G. R. Werner and D. A. Uzdensky, ApJL **843**, L27 (2017).
[30] D. Ball, L. Sironi, and F. Özel, Astrophys. J. **884**, 57 (2019), 1908.05866.
[31] D. A. Uzdensky, arXiv e-prints arXiv:2007.09533 (2020), 2007.09533.
[32] F. Guo, X. Li, H. Li, W. Daughton, B. Zhang, N. Lloyd-Ronning, Y.-H. Liu, H. Zhang, and W. Deng, ApJ **818**, L9 (2016), 1511.01434.
[33] G. R. Werner, D. A. Uzdensky, M. C. Begelman, B. Cerutti, and K. Nalewajko, MNRAS **473**, 4840 (2018).
[34] D. Ball, L. Sironi, and F. Özel, ApJ **862**, 80 (2018).
[35] M. Petropoulou, L. Sironi, A. Spitkovsky, and D. Giannios, ApJ **880**, 37 (2019).
[36] E. G. Blackman and G. B. Field, Phys. Rev. Lett. **73**, 3097 (1994), astro-ph/9410036.
[37] P. Dmitruk, W. H. Matthaeus, and N. Seenu, Astrophys. J. **617**, 667 (2004).
[38] J. T. Dahlin, J. F. Drake, and M. Swisdak, Physics of Plasmas **21**, 092304 (2014), 1406.0831.
[39] S. Dalena, A. F. Rappazzo, P. Dmitruk, A. Greco, and W. H. Matthaeus, Astrophys. J. **783**, 143 (2014), 1402.3745.
[40] L. Comisso and L. Sironi, Astrophys. J. **886**, 122 (2019), 1909.01420.
[41] M. E. Rowan, L. Sironi, and R. Narayan, ApJ **850**, 29 (2017).
[42] D. A. Uzdensky, N. F. Loureiro, and A. A. Schekochihin, PhRvL **105**, 235002 (2010).
[43] Y.-H. Liu, F. Guo, W. Daughton, H. Li, and M. Hesse, PhRvL **114**, 095002 (2015).